RSC Advances

ROYAL SOCIETY OF CHEMISTRY

PAPER

View Article Online
View Journal | View Issue

Cite this: *RSC Adv.*, 2022, **12**, 8423

Enhanced performance in uncooled n-CdSe/p-PbSe photovoltaic detectors by high-temperature chloride passivation

Yingmin Luo,[a] Lance McDowell,[b] Leisheng Su,[a] Yun Liu,[a] Jijun Qiu *[a] and Zhisheng Shi *[b]

High-temperature chloride passivation (HTCP) was proposed to improve the crystalline quality and electrical properties of PbSe epitaxial films. The PL intensity of HTCP (111) PbSe epitaxial films exhibits a 14 times higher intensity than that of as-grown films, and a threefold increase in Hall mobility has been obtained after HTCP at 300 °C for 2 h. The improvement of optical and electrical properties is attributed to the high-temperature defect passivation induced by the HTCP process. The HTCP process of PbSe films was implemented in a CdSe/PbSe heterojunction PV detector, which exhibits a room temperature peak detectivity D^* of 8.5 × 10^8 cm $Hz^{1/2}$ W^{-1} in the mid-wavelength infrared region under blackbody radiation (227 °C), demonstrating potential applications in the fabrication of mid-infrared detectors and emitters.

Received 23rd January 2022
Accepted 26th February 2022

DOI: 10.1039/d2ra00483f

rsc.li/rsc-advances

1. Introduction

Lead selenide PbSe, being sensitive to mid-infrared wavelengths (MWIR, 3–5 μm) at room temperature, is a promising active material for optoelectronic devices, including high-sensitivity infrared (IR) photodetectors,[1] IR-emitting diodes[2] and lasers.[3] It is widely accepted that an uncooled PbSe focal plane array (FPA) detector is the most cost-effective solution for multiple applications based on the detection of IR radiation.[4] The utilization of the uncooled photoconductive (PC) PbSe detectors can be traced back to the mid-1960s, and still to this day offers some great advantages for military, commercial and medical applications due to their low-cost and comparable performance to their counterparts such as $Hg_{1-x}Cd_xTe$ (MCT) at room temperature.[5–7] For example, Northrop-Grumman has developed a 320 × 240 staring PbSe FPA imaging system by modifying the standard chemical bath deposition (CBD) technology.[8] In 2007, G. Vergara developed a new vapor phase deposition (VPD) PbSe technology and demonstrated for the first time a 128 × 128 MWIR PbSe detector monolithically integrated with the corresponding Si-CMOS circuitry.[9]

However, its lower responsivity (D^*) and smaller format have been putting PbSe FPA detectors at a disadvantage in competition with MCT for 30 years. The lower D^* is mainly caused by a poor understanding of the complex physics involved in the photoconduction process in PbSe poly-crystals.[10–12] The poorer uniformity in photo-response and shorter-term stability of photosensitive CBD PbSe films suffering from the oxygen or iodine sensitization process restrict the pixel size and format of arrays.[13–15]

Theoretically, these disadvantages of uncooled PbSe PC FPA detectors could be overcome by adopting a single-crystalline photovoltaic (PV) junction device configuration based on molecular beam epitaxy (MBE) technology, such as n-PbSe/p-PbSe homojunction and Pb/p-PbSe Schottky.[16] MBE PbSe epitaxial films grown on silicon substrates have attracted more attention for large format FPA uncooled imaging applications, not only due to their large area uniformity and integration ability with Si wafer, but also extended photosensitive wavelength to long-IR range (8–12 μm) by Sn doping.[17–20] Based on these advantages, Shi explored an n-CdS/p-PbSe heterojunction device configuration by combining the CBD and MBE technologies.[17] However, the device performance is lower than both the theoretical limit and the PbSe PC detectors' performances, which is limited by high Shockley–Read Hall recombination associated with high dislocation density (>10^8 cm^2) and high carrier concentration (typical 5 × 10^{17} cm^{-3}) caused by large mismatch in lattice constant and coefficient of thermal expansion between lead-salt films and Si substrates.[19]

Many approaches have been carried out over the past several decades to eliminate or reduce those defects, including buffer layer and strained layer techniques,[17] lateral growth, selected area growth,[21,22] and *ex situ* annealing passivation techniques,[23] such as oxygen (O_2),[24,25] calcium difluoride (CaF_2),[26] native sulfide[27] and halide ions passivation.[28,29] Among them, high-temperature (>300 °C) oxygen passivation annealing (HTOP) is a near-optimum solution for a PV detector performance

[a]*School of Microelectronics, Dalian University of Technology, Dalian, PR China 116024. E-mail: jjqiu@dlut.edu.cn*

[b]*School of Electrical and Computer Engineering, University of Oklahoma, Norman, Oklahoma 73019, USA. E-mail: shi@ou.edu*

breakthrough.[23–25,30] Unfortunately, the HTOP process will destroy the surface flatness and uniformity of MBE-PbSe epitaxial films,[24,25] limiting its application in the field of PV PbSe FPA detectors.

To avoid surface degradation, in this letter, a new post annealing process named as high-temperature chloride passivation (HTCP) was proposed to improve the crystalline quality of MBE PbSe films, leading to enhanced MBE PbSe PV detector performance. Subsequently, the HTCP-PbSe films were utilized to form PV detectors with n-type CdSe films, which were synthesized from thermal evaporation method. Comparing with n-CdS, it is believed that CdSe has a better potential to form a stronger heterojunction interface with PbSe due to the presence of the same anion (Se^{2-}). By optimization of materials and process, a specific detectivity (D^*) of 8.5×10^8 cm $Hz^{1/2}$ W^{-1} was obtained under zero-bias photovoltaic mode.

2. Experiment

2.1 Fabrication of materials and assembly of PV detector

2.1.1 Fabrication of p-PbSe epitaxial layer. PbSe thin film growth was performed on a 3-inch Si (111) substrate in a customized three growth-chamber molecular beam epitaxy (MBE) system. The double polished high resistant Si wafer was cleaned by a modified Shiraki cleaning method prior to the growth. After cleaning, the wafer was quickly dried by high purity N_2 gas purge and transferred into the MBE system. To obtain a high quality PbSe thin film on Si wafer, 2 nm CaF_2 was grown in the first growth chamber as a buffer layer at 800 °C. Then 1.2 μm PbSe film was deposited in the second growth chamber with a growth rate of 25 nm min^{-1} at 390 °C. An additional Se source was used to adjust the p-type carrier concentration of the film and also to ensure the material quality due to the high Se vapor pressure during growth.

2.1.2 Treatment of HTCP process. Thermal evaporation (TE) method was employed in our case for its good compactness and homogeneity. TE-$CdCl_2$ coating is of more compact and smooth structure than $CdCl_2$ film fabricated from wet-chemical spin-coating technology, showing outstanding uniformity and reproducibility. The dense TE-$CdCl_2$ film helps to prevent oxygen from damaging the surface of the epitaxial layer during the high-temperature passivation process. 1 μm $CdCl_2$ film was deposited over the p-PbSe epitaxial layer with a 30 nm min^{-1} rate by thermal evaporation at room temperature at 6×10^{-4} Pa. Then, the $CdCl_2$/PbSe film was treated at atmospheric pressure in a flow-through furnace at 200–400 °C for 5–30 min. A continuous gas flow of 100 sccm of Ar was used for the whole duration of the annealing process. Subsequently, the residual $CdCl_2$ was removed with 0.03 M HNO_3 aqueous solution in ultrasonic for 1 min, then rinsed thoroughly with deionized water and dried with N_2.

As a reference, ZnO films were deposited over MBE-PbSe epitaxial films *via* RF magnetron sputtering. A high purity (99.99%) ZnO target of 76.2 mm diameter was used for the deposition. The vacuum chamber was first evacuated to 5×10^{-4} Pa before the introduction of argon as the sputtering gas. The deposition was carried out at a pressure of 2.0 Pa in room temperature. The sputtering power was maintained at 200 W during deposition for 200 nm thickness.

2.1.3 Deposition of n-CdSe layer. CdSe film by thermal evaporation technique using a 99.99% purity source in a vacuum with an initial background pressure of 2×10^{-4} Pa. The substrate was kept at 200 °C. The obtained 300 nm thick films were monitored by a crystal monitor at 10 nm min^{-1}.

2.1.4 Assembly of PbSe PV detectors. The schematic configuration of CdSe/PbSe PV detector is shown in Fig. 1.

A photoresist (AZ5241E) layer was coated onto CdSe/PbSe layer by spin-coating at 2500 rpm for 60 s followed by a soft bake for 90 s at 95 °C. Then, quadrate photoresist arrays with 200×200 μm were patterned by using an MJB3 mask aligner UV lithography (275 W) with an exposure time of 10 s, followed by a development time of 45 s. Subsequently, the patterned CdSe arrays on PbSe film were fabricated by 10 s wet chemical etching and acetone life off. The etchant consists of equal parts of 80% H_3PO_4, 29% HCl, and H_2O. Next, electrode pattern was shaped by a second lithographic process, including a spin-coating at 2500 for 60 s, a soft bake at 95 °C for 90 s, UV exposure for 5 s, a hard bake at 120 °C for 90 s, a UV exposure for 50 s, and development for 60 s. Then, 50 nm indium (In) and 200 nm Au electrode were deposited in turn by employing thermal evaporation at room temperature for 10 min in 2×10^{-4} Pa. Finally, 200×200 μm Au/In electrodes on the CdSe arrays were obtained after lift-off in acetone solvent for 5 min.

2.1.5 Measurement methods. The electrical properties (including carrier concentration and mobility) of PbSe thin films were determined by Hall effect measurements in van der Pauw four-point probe configuration, using fresh indium contacts, in an automated EGK HEM-2000 Hall Effect measurement system with a magnetic induction of 0.37 T. The photoluminescence (PL) with a Nd:YAG pulse pumping laser was measured by the Bruker IFS 66/S FTIR spectrometer. The morphology of PbSe films were characterized by a Zeiss Neon-40 EsB high-resolution field-emission scanning electron microscope (FESEM). The room temperature dark current density *versus* voltage (*J*–*V*) characteristic of the heterojunction device was performed by using Keithley 2400 source meter in the bias range from −1 to 1 V. The detector performance was then evaluated by a homemade detectivity measurement system. In this system, a calibrated 800 K blackbody from Infrared System Development was used as the standard infrared light source. A Thorlabs MC1F10 mechanical chopper was integrated to

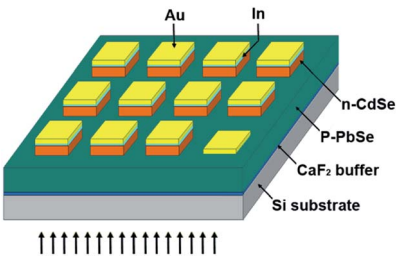

Fig. 1 Schematic configuration of CdSe/HTCP-PbSe PV detector structure.

provide a frequency modulated heat source. The heterojunction diode was operated in photovoltaic mode with zero applied bias during the measurement. Without connecting to any preamplifier, signal and noise currents from the device were directly collected by a Stanford Research System SR830 lock-in amplifier.

3. Results and discussion

3.1 Theory

$CdCl_2$ was selected to passivate the PbSe films based on the following four reasons. Firstly, the Cl substitutionary action on the Se sublattice leaves undisturbed the conduction band of PbSe that consists primarily of Pb orbitals.[31] Secondly, it was confirmed that $CdCl_2$ can effectively decrease the defect density of PbSe quantum dots as hybrid passivation scheme.[32] Third, $CdCl_2$ could be easily removed by low-cost wet-chemical etching method, and the etching does not cause any damage on the PbSe surface. Fourth, high temperature $CdCl_2$ treatment is a key processing step identified in the late 1970s to drastically improve the solar to electric conversion efficiency of CdS/CdTe solar cells by passivating a large number of columnar grain boundaries and decreasing the intrinsic or native defects in CdS and CdTe layers.[33–37]

The Cl diffusion and substitutionary in PbSe is assumed in a thermodynamic equilibration and is mediated by using a "concerted-exchange" process in which the dopant atom and one of its nearest-neighboring atoms swap places. Therefore, the activation temperatures could be calculated by a simple Arrhenius behavior:[38]

$$\nu_{\mathrm{diff}} = \nu^{0}_{\mathrm{diff}} \exp\left(-\frac{E_{\mathrm{diff}}}{kT}\right) \quad (1)$$

where ν_{diff} is the reaction rate, assuming $\nu_{\mathrm{diff}} = 1\ \mathrm{s}^{-1}$, ν^{0}_{diff} is the bare attempt frequency (typical of $10^{13}\ \mathrm{S}^{-1}$), E_{diff} is the diffusion energy, which is the energy of the transition state relative to the energy of the initial state. The theoretical E_{diff} for Cd, Cl, Pb and Se in bulk PbSe is 2.74, 1.35, 1.2 and 0.82 eV, respectively, according to the density-functional theory (DFC) calculations by Steven C. Erwin *etc.*[39–41]

Fig. 2 shows the theoretical diffusion temperature values in the light of above data, 789 °C for Cd and 254 °C for Cl. For a controllable diffusion rate, therefore, the heat-treatment temperature was limited below 400 °C, marked in yellow.

3.2 Experimental results and discussion

Photoluminescence spectrum (PL) is considered to be an effective quality inspection technique by comparing the intensity of optical photoluminescence peaks. Fig. 3 shows the room temperature PL spectra of PbSe films that underwent HTCP at different annealing temperatures for an optimized time. In comparison, the RT PL spectrum for the as-grown MBE-PbSe film was given in Fig. 3a. It is obvious that the PL intensities were significantly enhanced as the annealing temperature increased, and maximum PL intensity was obtained at 300 °C (Fig. 3c), which is 14 times higher in comparison with the as-grown film. The subsequent experiments indicated that the enhanced intensity is due to the decreased defect density in PbSe films, which are attributed to the intrinsic-defect passivation caused by thermal annealing and the non-intrinsic defect passivation caused by Cl diffusion.[24,25]

To calculate the contribution percentage from the Cl^{-} non-intrinsic defect passivation, the PL of annealed PbSe epitaxial film covered with ZnO film was investigated, as shown in Fig. 3(e). The slight PL increase from ZnO coated MBE-PbSe film is only attributed to the thermal intrinsic defect passivation because for the following two reasons: (1) the Cl and O non-intrinsic compensation from the external environment were completely blocked by the dense ZnO film; (2) oxygen in ZnO unit cells couldn't produce any contribution to the non-intrinsic defect passivation due to a huge Zn–O bond strength of 150.6 KJ mol^{-1}.[42,43] Therefore, the contribution percentage from the non-intrinsic defect passivation P_{NIP} (%):

$$P_{\mathrm{NIP}}\ (\%) = \frac{\mathrm{PL}_{\mathrm{CdCl_2}} - \mathrm{PL}_{\mathrm{ZnO}}}{\mathrm{PL}_{\mathrm{CdCl_2}}} \quad (2)$$

where $\mathrm{PL}_{\mathrm{CdCl_2}}$ and $\mathrm{PL}_{\mathrm{ZnO}}$ is the PL intensity of PbSe with HTCP and ZnO passivation, respectively. There is only a 1.6-fold increase in PL intensity under thermal intrinsic defect passivation, an 11% contribution for total enhancement. Therefore, we can now conclude that decreased defect density caused by the Cl^{-} non-intrinsic defect passivation is mainly responsible (89%) for the high PL of the annealed PbSe films. A 5-fold

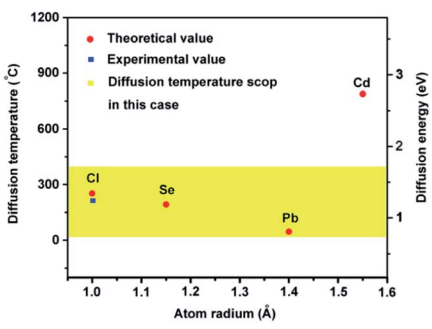

Fig. 2 The theoretical and experimental diffusion temperatures for Cl, Se, Cd and Pb.

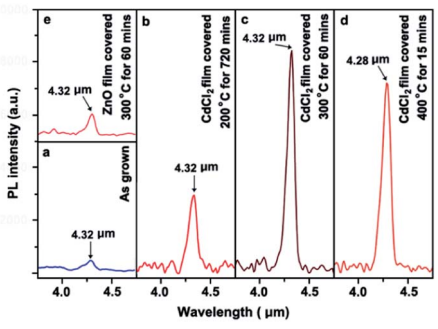

Fig. 3 PL spectra of PbSe films with $CdCl_2$ passivation at various temperature (a) as-grown MBE-PbSe film; (b) 200 °C; (c) 300 °C; (d) 400 °C; (e) reference sample.

increase in PL intensity was observed after annealing at 200 °C for 12 h, indicating the experimental activation temperature of Cl is lower than the theoretically calculated one (254 °C), and the experimental E_{diff} for Cl is 1.21 eV according to eqn (1). This is due to the large number of defects in MBE-PbSe films, instead of an ideal crystal utilized in the theoretical calculation. Besides the 11-fold increase in intensity, a 40 nm blue shift was also observed after annealing at 400 °C for 15 min.

The carrier concentration and mobility as a function of $CdCl_2$-treated temperature is shown in Fig. 4. The as-grown PbSe film was found to be p-type, and the carrier concentration was 3.4×10^{17} cm^3 at 77 K and 5.2×10^{17} cm^3 at room temperature (RT). After $CdCl_2$ passivation, the carrier concentration decreased with increasing the annealing temperature, and reached minimum value of 2.0×10^{17} cm^3 at 300 °C.

Subsequently, the carrier concentration almost bounced back to the original value at 77 K and RT. Furthermore, the semiconductor type of PbSe transferred from p-type to n-type as annealing temperature increased up to 400 °C. The transformation of semiconductor type is attributed to the occurrence of the interstitial Cl^- defects (i'_{Cl}) and the selenium evaporation from PbSe triggered by high temperature. The decrease of carrier concentration resulted from the intrinsic defect, such as selenium vacancies (V''_{Se}) passivated by Cl^- diffusing into the PbSe and occupying V''_{Se}, which is confirmed by the high carrier concentration of 4.1×10^{17} cm^3 at 300 K and 2.9×10^{17} cm^3 at 77 K of ZnO covered PbSe annealed at 300 °C for 1 h. Therefore, a decrease of nearly 65% in carrier concentration is attributed to the non-intrinsic defect passivation by Cl^- diffusion. At the same time, the mobilities have a maximum of 600 cm^2 V^{-1} s^{-1} at 300 K and 10 000 cm^2 V^{-1} s^{-1} at 77 K after 300 °C HTCP, increasing 2 times and 3 times more than free-Cl^- passivation samples, respectively. However, the mobility of $CdCl_2$-passivated PbSe epitaxial film maintains the same value with ZnO-covered samples annealed at 300 °C, indicating that thermal intrinsic defect passivation plays a key role in promoting the mobility of MBE PbSe epitaxial films. This result was further confirmed by the fact that mobilities of ZnO covered PbSe film research 1000 at 300 K and 30 000 cm^2 v^{-1} s^{-1} at 77 K after annealing temperature was increased to 400 °C. In addition,

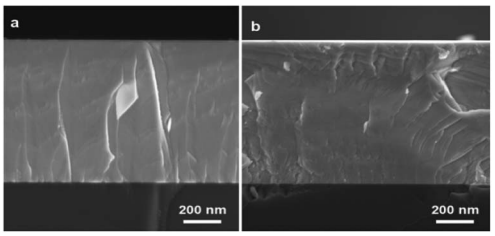

Fig. 5 FESEM images of PbSe epitaxial films. (a) Without, and (b) with HTCP.

there is no conducting type transition for ZnO-covered PbSe film until 450 °C, which further proves that lower conducting type transition temperature (400 °C) for $CdCl_2$-passivated PbSe mainly is attributed to the interstitial Cl^- defects (I'_{Cl}) being n-type dopants.

Although O_2 passivation can simply improve the quality of MBE-PbSe epitaxial films, the effective passivation temperature of >300 °C will severely damage the surface by forming an oxidation layer of $PbSeO_3$ and selenium evaporation.[25] The cross-view FESEM images of $CdCl_2$-passiviated PbSe epitaxial films annealed at 300 °C is shown in Fig. 5. It is obvious that no surface damage was observed after high-temperature passivation and wet-chemical etching process. The smooth surface and the improved electrical properties provide the necessary morphological structure and electrical band structure to build high-performance PbSe PV detectors (Fig. 6).

Being a direct bandgap II–VI semiconductor with an electronic affinity of 4.85 ± 0.1 eV,[44–46] CdSe combine with PbSe epitaxial film to form a type-II band alignment, which makes them suitable candidates for photovoltaics applications. An n-CdSe and p-PbSe p–n heterojunction PV detector was assembled to investigate the effects of HTCP on detector performance. The electrical characteristics of CdSe/PbSe photodiode without HTCP process has a 16.5 ON/OFF ratio, the reverse dark current of ~72 mA cm^{-2} at −1 V, and an ideal factor (n) of ~1.8. After the HTCP process, the reverse saturation current of the photodiode is 8 times lower than that free-HTCP photodiode at room temperature, and the ON/OFF ratio increases to 306. The decreased dark current of 9 mA cm^{-2} and the increased ON/OFF ratio are attributed to the improved crystal quality of PbSe epitaxial films after HTCP.

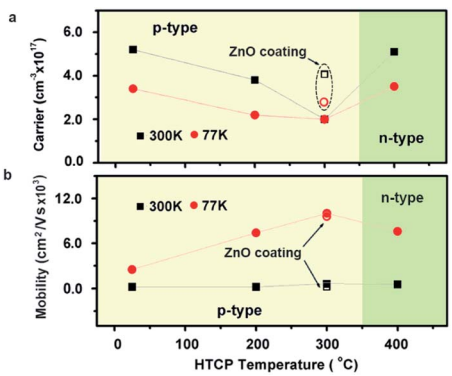

Fig. 4 Carrier concentration (a) and mobility (b) as a function of $CdCl_2$ annealing temperature.

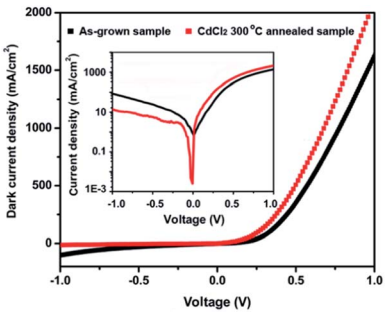

Fig. 6 Dark current density–voltage (J–V) characteristics of CdSe/PbSe PV detectors with HTCP.

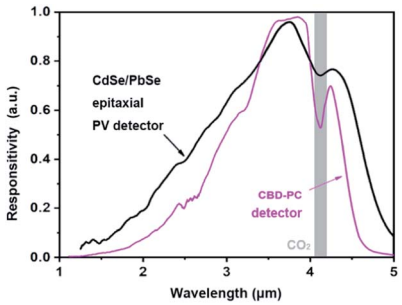

Fig. 7 Room-temperature spectral response curves of the CdSe/PbSe PV detector and CBD-PbSe photoconductive detectors.

A relative response spectrum of the CdSe/PbSe PV detector was measured using a Fourier transform infrared spectrometer at room temperature. It is clear that the photosensitive band of the detector with HTCP ranges from 1.0 to 5.0 μm, and reaches a maximum at 3.8 μm. The cut-off wavelength of the photodiode is approximately 4.6 μm, which is larger than that of polycrystal PbSe photoconductive detectors fabricated from the standard CBD method, as shown in Fig. 7. It is 300 nm red-shift of the cutoff wavelength that makes CdSe/PbSe heterojunction PV detectors widely available for gas sensing.

To further demonstrate the performance of the PV detector, photoelectric properties under blackbody illumination were subsequently investigated at room temperature. The blackbody detectivity (D^*) of the device is calculated in the following way. The noise of PV detectors is primarily induced by $1/f$ noise, shot noise, and thermal noise. To ignore the $1/f$ noise which dominates at low frequency, the CdSe/PbSe PV detector was measured at a modulation frequency of 750 Hz. In addition, zero-bias photovoltaic mode was employed to minimize both the shot noise and the thermal noise. Hence, the D^* could be calculated using the formula:

$$D^* = \frac{S\sqrt{\Delta f}}{NP\sqrt{A}}$$

where S is signal output, Δf is noise bandwidth (1 Hz), A is the detector active area, N is noise output, and P is incident energy, which can be calculated by following equation:

$$P = \frac{\alpha\sigma\left(T^4 - T_0^4\right)A_0}{\pi L^2}$$

where α is modulation factor of chopper, σ is Stefan–Boltzmann constant, T is temperature of blackbody, T_0 is room temperature, A_0 is aperture area of blackbody and L is distance between blackbody and detectors. In our detection system the value of α is 0.45, T is 500 K, T_0 is 300 K, A_0 is 0.0127 cm^2 and L is 20 cm. The measured room-temperature peak D^* reaches 8.5×10^8 cm $Hz^{1/2}$ W^{-1} in the MWIR region, which is more than 3 times performance of HTCP-free CdSe/PbSe detector. At the same time, the detectivity D^* of CdSe/PbSe detectors is higher than that of CdS/PbSe PV detectors in our previous report, proving the feasibility of using CdSe/PbSe heterostructure for mid-IR detection at room temperature.

4. Conclusion

In conclusion, high-temperature chloride passivation (HTCP) was proposed to improve the crystalline quality and electrical properties of PbSe epitaxial films by thermal intrinsic defect passivation and Cl^- non-intrinsic defect passivation. The PL intensity of the PbSe epitaxial film after undergoing HTCP at 300 °C exhibits a 14 times higher intensity than that of as-grown films. A threefold increase in Hall mobility was also obtained from HTCP at 300 °C. This simple HTCP process of PbSe films was implemented in the fabrication of CdSe/PbSe heterojunction PV detector, which demonstrated a significant device performance enhancement, with a peak detectivity D^* of 8.5×10^8 cm $Hz^{1/2}$ W^{-1} at 3.8 μm under zero-bias photovoltaic mode. HTCP shows a potential application in the fabrication of mid-infrared detectors and emitters.

Author contributions

J. Q. conceived the presented idea, carried out the materials growth, fabricated the detectors and performed the characterization. Y. L and L. M analysed the data and wrote the manuscript with support from L. S., Y. L. Both J. Q. and Z. S. contributed to the final version of the manuscript. Z. S. supervised the findings of this work.

Conflicts of interest

There are no conflicts to declare.

Acknowledgements

All conceptual and experimental work were completed at the University of Oklahoma, which was supported by the US DARPA WIRED program through Northrop Grumman, and US army research office (ARO) under contract no. W911NF-18-1-0418. The manuscript was completed at Dalian University of Technology, China. The writing of the manuscript was funded by the Dalian Science and Technology Innovation Fund (2020JJ26GX022) and Fundamental Research Funds for the Central Universities (Grant No. DUT19RC (3)032).

Notes and references

1 S. Roa, M. Sandoval and M. Sirena, *Mater. Chem. Phys.*, 2021, **264**, 124479.
2 J. Zhang, X. Liu, P. Jiang, H. Chen, Y. Wang, J. Ma, R. Zhang, F. Yang, M. Wang, J. Zhang and G. Tu, *Nano Energy*, 2019, **66**, 104142.
3 C. L. Felix, W. W. Bewley, I. Vurgaftman, J. R. Lindle, J. R. Meyer, H. Z. Wu, G. Xu, S. Khosravani and Z. Shi, *Appl. Phys. Lett.*, 2001, **78**, 3770–3772.
4 M. Kastek, T. Piątkowski, H. Polakowski, J. Barela, K. Firmanty, P. Trzaskawka, G. Vergara, R. Linares, R. Gutierrez, C. Fernandez and M. T. Montojo, *Proc. SPIE*, 2014, **9074**, 90740A.

5 Y. X. Ren, T. J. Dai, W. B. Luo and X. Z. Liu, *Vacuum*, 2018, **149**, 190–194.
6 J. Qiu, B. Weng, Z. Yuan and Z. Shi, *J. Appl. Phys.*, 2013, **113**, 103102.
7 F. Briones, D. Golmayo and C. Ortiz, *Thin Solid Films*, 1981, **78**, 385–395.
8 T. Beystrum, R. Himoto, N. Jacksen and M. Sutton, *Proc. SPIE*, 2004, **5406**, 287–294.
9 G. Vergara, L. J. Gómez, V. Villamayor, M. Álvarez, M. C. Torquemada, M. T. Rodrigo, M. Verdú, F. J. Sánchez, R. M. Almazán, J. Plaza, P. Rodriguez, I. Catalán, R. Gutierrez, M. T. Montojo, F. Serra-Graells, J. M. Margarit and L. Terés, *Proc. SPIE*, 2007, **6542**, 654220–654229.
10 C. Marcott, R. C. Reeder, J. A. Sweat, D. D. Panzer and D. L. Wetzel, *Vib. Spectrosc.*, 1999, **19**, 123–129.
11 V. Kasiyan, Z. Dashevsky, C. Minna Schwarz, M. Shatkhin, E. Flitsiyan, L. Chernyak and D. Khokhlov, *J. Appl. Phys.*, 2012, **112**, 86101.
12 R. L. Petritz, *Phys. Rev.*, 1956, **104**, 1508–1516.
13 R. Ahmed and M. C. Gupta, *Opt. Lasers Eng.*, 2020, **134**, 106299.
14 M. Jang, P. M. Litwin, S. Yoo, S. J. McDonnell, N. K. Dhar and M. C. Gupta, *J. Appl. Phys.*, 2019, **126**, 105701.
15 P. Kumar, M. Pfeffer, E. Schweda, O. Eibl, J. Qiu and Z. Shi, *J. Alloys Compd.*, 2017, **724**, 316–326.
16 H. Zogg, A. Fach, J. John, J. Masek, P. Mueller, C. Paglino and S. Blunier, *Opt. Eng.*, 1995, **34**, 1964–1969.
17 B. Weng, J. Qiu, L. Zhao, C. Chang and Z. Shi, *Appl. Phys. Lett.*, 2014, **104**, 121111.
18 M. T. Rodrigo, J. Diezhandino, G. Vergara, G. Perez, M. C. Torquemada, F. J. Sanchez, V. Villamayor, R. Almazan, M. Verdu, I. Genova, P. Rodriguez, L. J. Gomez, I. Catalan, J. Plaza and M. T. Montojo, *Detectors and Associated Signal Processing*, 2004, vol. 5251, pp. 97–102.
19 P. Muì Ller, A. Fach, J. John, A. N. Tiwari, H. Zogg and G. Kostorz, *J. Appl. Phys.*, 1996, **79**, 1911–1916.
20 X. Shi, Q. Phan, B. Weng, L. L. McDowell, J. Qiu, Z. Cai and Z. Shi, *Detection*, 2018, **06**, 1–16.
21 A. Osherov and Y. Golan, *MRS Bull.*, 2010, **35**, 790–796.
22 J. Chen, Q. Ma, X. Wu, L. Li, J. Liu and H. Zhang, *Nano-Micro Lett.*, 2019, **11**, 86.
23 X. Sun, K. Gao, X. Pang, H. Yang and A. A. Volinsky, *J. Mater. Sci.: Mater. Electron.*, 2016, **27**, 1670–1678.
24 F. Zhao, S. Mukherjee, J. Ma, D. Li, S. L. Elizondo and Z. Shi, *Appl. Phys. Lett.*, 2008, **92**, 211110.
25 F. Zhao, J. Ma, D. Li, S. Mukherjee, G. Bi and Z. Shi, *J. Electron. Mater.*, 2009, **38**, 1661–1665.
26 S. Mukherjee, D. Li, G. Bi, J. Ma, S. L. Elizondo, A. Gautam and Z. Shi, *Microelectron. Eng.*, 2011, **88**, 314–317.
27 C. Gautier, G. Breton, M. Nouaoura, M. Cambon, S. Charar and M. Averous, *J. Electrochem. Soc.*, 1998, **145**, 512–517.
28 A. C. Bouley, H. R. Riedl, J. D. Jensen and S. R. Jost, *US Pat.*, US4442446A, 1984.
29 M. Drinkwine, J. Rozenbergs, S. Jost and A. Amith, *Proc. SPIE-Int. Soc. Opt. Eng.*, 1981, **285**, 36–43.
30 K. Shi, Y. Liu, Y. Luo, J. Bian and J. Qiu, *RSC Adv.*, 2021, **11**, 36895–36900.
31 J. Androulakis, D. Y. Chung, X. Su, Z. Li, C. Uher, T. C. Hasapis, E. Hatzikraniotis, K. M. Paraskevopoulos and M. G. Kanatzidis, *Phys. Rev. B: Condens. Matter Mater. Phys.*, 2011, **84**, 564–576.
32 A. H. Ip, S. M. Thon, S. Hoogland, O. Voznyy, D. Zhitomirsky, R. Debnath, L. Levina, L. R. Rollny, G. H. Carey, A. Fischer, K. W. Kemp, I. J. Kramer, Z. Ning, A. J. Labelle, K. W. Chou, A. Amassian and E. H. Sargent, *Nat. Nanotechnol.*, 2012, **7**, 577–582.
33 W. K. Metzger, D. Albin, M. J. Romero, P. Dippo and M. Young, *J. Appl. Phys.*, 2006, **99**, 103703.
34 A. R. Marshall, M. R. Young, A. J. Nozik, M. C. Beard and J. M. Luther, *J. Phys. Chem. Lett.*, 2015, **6**, 2892–2899.
35 E. Regalado-Pérez, M. G. Reyes-Banda and X. Mathew, *Thin Solid Films*, 2015, **582**, 134–138.
36 R. W. Crisp, D. M. Kroupa, A. R. Marshall, E. M. Miller, J. Zhang, M. C. Beard and J. M. Luther, *Sci. Rep.*, 2015, **5**, 9945.
37 M. J. Kim, J. J. Lee, S. H. Lee and S. H. Sohn, *Sol. Energy Mater. Sol. Cells*, 2013, **109**, 209–214.
38 E. Ko, M. M. G. Alemany and J. R. Chelikowsky, *J. Chem. Phys.*, 2004, **121**, 942–945.
39 S. C. Erwin, *Phys. Rev. B: Condens. Matter Mater. Phys.*, 2010, **81**, 235433.
40 F. D. Ott, L. L. Spiegel, D. J. Norris and S. C. Erwin, *Phys. Rev. Lett.*, 2014, **113**, 156803.
41 A. Kutana and S. C. Erwin, *Phys. Rev. B: Condens. Matter Mater. Phys.*, 2011, **83**, 235419.
42 T. Honma, Y. Benino, T. Komatsu, R. Sato and V. Dimitrov, *Phys. Chem. Glasses*, 2002, **43**, 32–40.
43 K. SUN, *J. Am. Ceram. Soc.*, 1947, **30**, 277–281.
44 V. Stevanovi, S. Lany, D. S. Ginley, W. Tumas and A. Zunger, *Phys. Chem. Chem. Phys.*, 2014, **16**, 3706–3714.
45 S. Kasap and P. Capper, *Springer handbook of electronic and photonic materials*, 2nd edn, 2017.
46 Ya. I. Lepikh, I. A. Ivanchenko and L. M. Budiyanskaya, *Semicond. Phys., Quantum Electron. Optoelectron.*, 2014, **17**, 408–411.